*Geophys. J. Int.* (2008) **173,** 740–750 doi: 10.1111/j.1365-246X.2008.03737.x

# Three-dimensional modelling of magnetotelluric data from the Rotokawa geothermal field, Taupo Volcanic Zone, New Zealand

W. Heise, T. G. Caldwell, H. M. Bibby and S. C. Bannister

*GNS Science,* 1*, Fairway Drive,* PO Box 30368*, Lower Hutt, New Zealand. E-mail: w.heise@gns.cri.nz*

Accepted 2008 January 15. Received 2008 January 14; in original form 2007 September 10

## SUMMARY

The resistivity structure of the Rotokawa geothermal system in New Zealand's Taupo Volcanic Zone has been determined by 3-D modelling of data from a closely spaced (64 measurement sites) magnetotelluric (MT) survey. 3-D conductivity models were constructed using trial and error forward modelling of the phase-tensor data and 3-D inverse modelling of the impedance tensor data. Both the forward and the inverse resistivity models show good consistency. The most interesting feature of these models is a resistive (∼100 Ωm) zone within the otherwise conductive material of the geothermal system. This zone coincides with the high temperature (300–335 °C) core of the geothermal system in which seismicity induced by fluid injection occurs and may mark the zone of fracture permeability that is feeding high temperature fluid into the geothermal system from deeper levels.

**Key words:** Electrical properties; Magnetotelluric; Hydrothermal systems.



## INTRODUCTION

The Taupo Volcanic Zone (TVZ, Fig. 1) contains all but one of New Zealand's high temperature (>200 °C) geothermal systems. These systems have been extensively investigated since the 1960's using a variety of different geophysical exploration methods (Risk 1983). The most effective exploration methods applied by far was direct current (DC) apparent resistivity mapping (Bibby 1988). These data, which provide a map (Fig. 1) of the resistivity distribution of the TVZ down to depths of ∼500 m (Bibby *et al.* 1995), played a vital role in delineating geothermal systems and in stimulating the development of New Zealand's geothermal electric power industry.

The effectiveness of the DC resistivity mapping for geothermal exploration in the TVZ arises from the large resistivity contrast between hot, hydrothermally altered material within the geothermal fields and the unaltered, young rhyolitic-volcanics that surround them. Each of the low resistivity (red) areas shown in Fig. 1 marks the near-surface expression of a large convective plume of hot water that rises to the surface from near the brittle ductile transition, ∼7–8 km below the surface. The total convective heat output discharged from the TVZ's geothermal field is 4200 MW (Bibby *et al.* 1995).

In the early stages of development, economically useful production of hot water from the TVZ's geothermal fields was obtained from production wells less than 1500-m deep, in many cases less than 1000 m. However, production from such shallow depths produces detrimental environmental effects by changing the near-surface hydrology of the geothermal systems. These effects can be mitigated to some degree by obtaining higher temperature geothermal fluid from deeper levels. This reduces the amount of fluid needed for power production and helps separate the impact of production from the near-surface hydrology.

Knowledge about the TVZ's geothermal reservoirs, i.e. the deep (>1500 m deep) high-temperature parts of the geothermal systems, comes mainly from drill holes, as geophysical exploration techniques have not been able to clearly resolve structures below this level (i.e. below ∼1500 m). For example, seismic reflection surveys that are highly successful in a sedimentary environment have been singularly unsuccessful in the TVZ because of severe attenuation and reverberation in the surface layer of recent volcanics (Bannister & Melhuish 1997).

Here we report the results of a detailed MT survey of the Rotokawa geothermal system, conducted in an attempt to explore its deeper structure. Currently Rotokawa produces 33 MW of electric power using fluid from four production wells, although the power capacity of the field is much greater. Several deep wells (>2 km) have been drilled within the geothermal field, encountering temperatures exceeding 330 °C, which are among the highest *in situ* temperatures measured in the TVZ (e.g. Hunt & Harms 1990).

Previous investigations of the deep resistivity structure at Rotokawa (Risk 2000) used long-offset bipole–dipole tensor resistivity techniques (Bibby 1986; Bibby & Hohmann 1993). In principle, the detection depth of a DC bipole–dipole measurement is determined by the source–receiver offset. In practice, the detection depth is limited by the size of the grounded-bipole source-moment and electrical noise at the receiver. Data obtained using this DC technique provided the confirmation needed that the shallow low-resistivity areas mapped in the Schlumberger surveys were not just superficial features. A further important result of the bipole–dipole surveys was the recognition that the deeper parts of the geothermal system are more resistive at depth than their upper parts, although the geothermal system as a whole is still more conductive than the surrounding material (e.g. Bibby & Risk 1973).

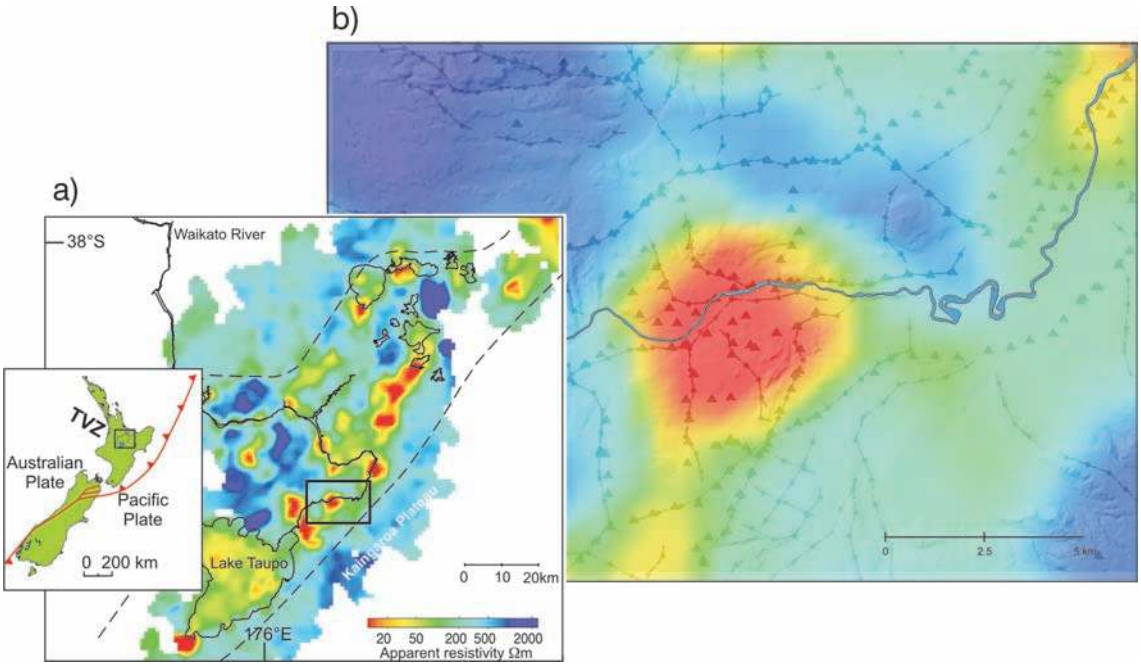


**Figure 1.** (a) DC apparent resistivity map from Bibby *et al.* (1995). Dashed lines show the approximate outline of the TVZ in the area containing (mainly rhyolitic) volcanism <2-Ma old. Conductive areas shown in red (<30 Ωm) mark the geothermal systems. (b) Schlumberger apparent resistivity map made with an electrode spacing of (AB/2) 500 m of the Rotokawa area. Background symbols show DC apparent resistivity measurement sites (Bibby 1988).

Detailed interpretation of DC bipole data is difficult because the resistivity structure must be inferred from the spatial changes in the observed electric field and lack the third dimension provided by (time-domain) transient electromagnetic or (frequency domain) magnetotelluric (MT) surveys. Pellerin *et al.* (1996) conducted an evaluation of EM methods for geothermal exploration using 3-D numerical models based on a geological model of conductivity structure. In this evaluation, the increase in resistivity in the higher temperature parts of the geothermal system included in their models is attributed to a change in the type of hydrothermal alteration products from highly conductive to less-conductive clay minerals discussed in more detail later.

Pellerin *et al.* (1996) examined the ability of different EM methods to reliably detect the deep geothermal reservoir beneath a thick highly conductive 'clay-cap' at the top of the geothermal reservoir. They concluded that long-offset transient electric field and MT measurements offered the best approach to this problem. In this paper, we will present the results of 3-D forward and inverse modelling of a detailed MT survey of the geothermal system using visualization techniques based on the MT phase tensor (Caldwell *et al.* 2004) to illustrate and compare the modelling results.

## GEOLOGICAL SETTING

The TVZ is an active continental rift system characterized by voluminous rhyolitic volcanism less than 1.6-Ma old (Wilson *et al.* 1995). The uppermost 1–3 km of the TVZ are composed mainly of a mixture of rhyolitic lavas, ignimbrites (both welded and unwelded) and volcaniclastic sediments. Along the SE margin of the TVZ the basement rocks (Mesozoic greywacke meta-sediments) dip ∼20° to the NW beneath the rhyolitic volcanics (Bibby *et al.* 1998). The Rotokawa geothermal field is located adjacent to the SE margin of the TVZ where the basement rocks have been down-faulted along major normal faults that strike SW–NE. At Rotokawa, andesites were encountered in drill holes at depths of between 1 and 2 km, directly overlying the basement greywacke (Arehart *et al.* 2002).

## RESISTIVITY STRUCTURE

Near the surface, the (recent) volcanic material is resistive (≥300 Ωm). However, at deeper levels, the rhyolitic volcanics become conductive (10–30 Ωm) due to a diagenetic aging process in which small amounts of conductive clays and zeolites form within the volcanics (Stanley *et al.* 1990; Bibby *et al.* 2005b). Thus, outside the geothermal systems, the conductivity depth structure of the TVZ is characterized by a layer of young, resistive volcanics overlying a layer of much more conductive older volcanics. Basement greywacke, which lies beneath a thin veneer of ignimbrite in the southeast is resistive ∼1500 Ωm (Bibby *et al.* 1998). Within the TVZ, Heise *et al.* (2007) showed that the basement greywacke is similarly resistive except in a 10-km-wide strip along the southeast margin of the TVZ where the resistivity of the greywacke is significantly less (∼200 Ωm).

The near-surface low resistivities seen in the Schlumberger resistivity data (Fig. 1) inside the geothermal fields are caused by the combination of hydrothermal alteration of the young volcanics and higher temperature and saline (or acidic) fluid. At depths greater than ∼500 m, the resistivity values increase due to decreasing pore space and a change in the type of hydrothermal alteration products (clays), produced by the interaction of geothermal fluids with the volcanic rocks. At higher temperatures, the alteration products are less-conductive illitic and chloritic clays rather than smectite, which is unstable at high temperatures (Björnsson *et al.* 1986; Ussher *et al.* 2000). Thus the higher temperature parts of the geothermal system are marked by somewhat higher resistivities beneath a cap of highly conductive clays produced by hydrothermal alteration at shallow levels within the geothermal system. In contrast, outside the geothermal systems, resistivity decreases with increasing depth.

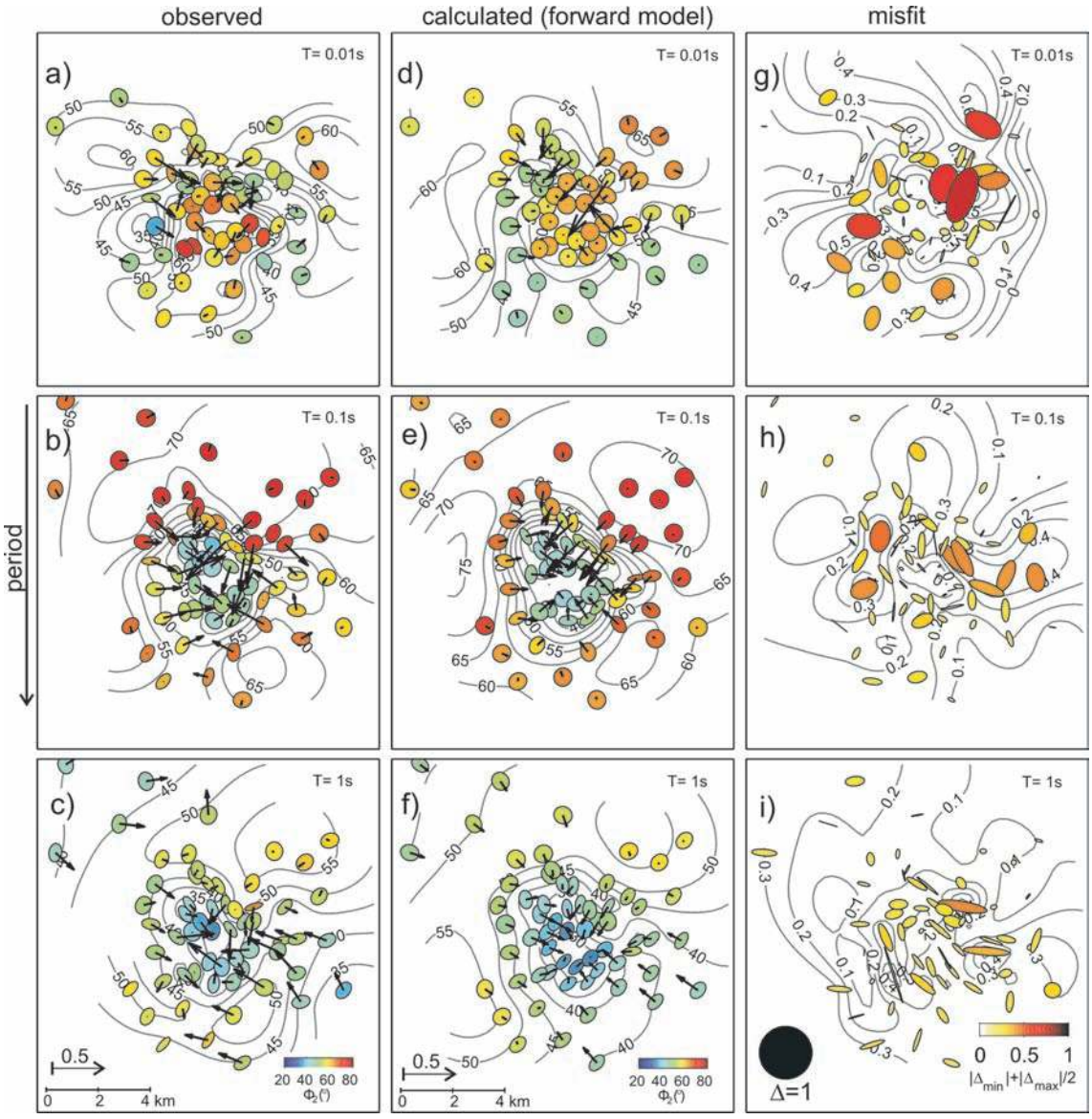


**Figure 2.** (a–c) Phase-tensor ellipses and real induction arrows (eq. 2) between 0.01 s and 1 s. The ellipses are normalized with $\Phi_{max}$ and the colours show $\Phi_2 = \sqrt{\Phi_{min}\Phi_{max}}$. The high values of $\Phi_2$ outside the geothermal system indicate decreasing resistivity with depth caused by more conductive older volcaniclastics beneath a surface layer of young resistive volcanics. Note the low phase values in the centre of the geothermal system for 0.1 and 1 s, indicating increasing resistivity with depth. Induction arrows, which point in the direction of increasing conductance, show the strong conductivity contrast at shallow depths. (d–f) Calculated phase response from the 3-D forward model, main features of the data, are reproduced at all periods. (g–i) Tensor misfit ellipses ($\boldsymbol{\Delta}$) calculated for the observed and calculated phase tensors. The colour used to fill the ellipses shows the mean of the maximum and minimum misfit: $(|\Delta_{max}|+|\Delta_{min}|)/2$. Small and light coloured ellipses indicate that the misfit is small.

## MAGNETOTELLURIC DATA

The locations of the 64 broadband (0.3 ms–2000 s) MT soundings used for the forward modelling are shown in Fig. 2. Data processing was carried out using robust, remote-reference signal processing techniques (Larsen *et al.* 1996). In the central part of the geothermal field, i.e. in the area characterized by the low Schlumberger apparent resistivities (Fig. 1), the spacing between measurement sites is between 200 and 500 m. The 'aperture' of the MT survey at Rotokawa is about 10-km wide, which in principle allows determination of the (3-D) resistivity structure down to depths of ∼5 km.

MT data are represented mathematically in the frequency domain by a complex 'impedance tensor' or 'transfer function' $\boldsymbol{Z}$, defined by the linear relation

$$\mathbf{E} = \boldsymbol{Z}\mathbf{H} \tag{1}$$

between the horizontal electric ($\mathbf{E}$) and magnetic ($\mathbf{H}$) field vectors. Essentially $\boldsymbol{Z}$, which contains the information about the resistivity structure, normalizes the electric field vector for the strength of the magnetic field fluctuation that induces the electric current in the earth. A similar complex transfer function between horizontal and vertical ($H_z$) magnetic field components is used to represent the vertical magnetic field information, where the equation

$$H_z = -\mathbf{K}\mathbf{H} \tag{2}$$

defines the induction vector **K**. (The sign of **K** has been chosen so that the induction vector points in the direction of increasing conductance following Parkinson (1962)

In a 1-D or 2-D situation, MT data are usually presented as the magnitude (apparent resistivity)

$$\rho_{kl} = \mu_o \omega |Z_{kl}|^2 \tag{3}$$

(where $\omega$ is the angular frequency) and phase

$$\phi_{kl} = \arg(Z_{kl}) \tag{4}$$

of the antidiagonal components of the impedance tensor in a coordinate system aligned with the strike of the resistivity structure. For 3-D conductivity structures the information contained in the diagonal elements of the impedance tensor has to be taken into account, making visualization of the MT data much more difficult. In particular, there is no single preferred or natural coordinate system in which to represent the data. The situation is further complicated by the effect of small-scale (i.e. less than the measurement spacing) resistivity structure near the surface that distorts the magnitude of the MT data (e.g. Jiracek 1990). However, by using only the phase information this latter problem can be avoided.

We use the phase tensor (Caldwell *et al.* 2004) and its coordinate invariants to visualize the observed and calculated data. The phase tensor (which is real) is defined by the relation

$$\boldsymbol{\Phi} = \boldsymbol{X}^{-1}\boldsymbol{Y}, \tag{5}$$

between $\boldsymbol{X}$ and $\boldsymbol{Y}$, which are the real and imaginary parts of the impedance tensor, respectively. Graphically, the phase-tensor can be represented as an ellipse with the principal axes ($\Phi_{\max}$ and $\Phi_{\min}$, respectively) showing the major and minor axes of the tensor. It is easy to show the phase tensor is independent of galvanic distortion (Caldwell *et al.* 2004), i.e. the frequency independent part of the observed electric field produced by localized small-scale resistivity heterogeneities. Representation of the MT data as phase-tensor maps provides a distortion-free method of visualizing the conductivity gradients of the subsurface and allows identification of the major features of the conductivity structure prior to modelling.

## MT RESULTS

Figs. 2(a–c) show maps of phase-tensor ellipses and real induction vectors at three selected periods. Data points with very large errors have been omitted from the maps. In all, usable MT data were recovered from 64 sites although at a few sites the amount of useable data was limited to short and long periods, where the MT signal strength is greatest.

The colour used to fill the ellipses in Figs 2(a–f) shows the geometric mean of the maximum and minimum phase

$$\Phi_2 = \sqrt{\Phi_{\max}\Phi_{\min}}, \tag{6}$$

which is coordinate invariant. Geometrically, this parameter is the radius of a circle that has the same area as the ellipse and provides a measure of the phase averaged over polarization direction.

At short periods (0.01 s, Fig. 2a), the phase-tensor ellipses are nearly circular except for sites close to the boundary separating the low resistivities inside the geothermal field from the surrounding area. Apart from the boundary region, this suggests that the near-surface resistivity structure is approximately 1-D. High $\Phi_2$ values ($>50^\circ$) inside the geothermal system indicate that the conductivity near the surface increases rapidly with depth.

Inside the geothermal system (Figs. 2b and c), $\Phi_2$ is $<45^\circ$ at both 0.1 and 1 s indicating increasing resistivity with depth. In contrast outside the geothermal system, phases are high at 0.1 s (Fig. 2b), showing that beneath the surface layer of high-resistivity volcanics resistivities decrease with depth, but increase again at depth as is shown by the low phase at longer periods (Fig. 2c). The phase-tensor maps show that the orientations of the principal axes of the ellipses vary spatially, indicating that the structure is strongly 3-D.

## 3-D FORWARD MODELLING

The near-surface resistivity structure of the geothermal system is known from the DC resistivity mapping (Fig. 1). Long-offset tensor resistivity studies (Bibby *et al.* 1998; Risk 2000) and regional MT studies (Ogawa *et al.* 1999; Heise *et al.* 2007) show a SW–NE striking regional conductivity structure, reflecting the down faulting of the greywacke basement along the southeastern rift margin. This information, along with knowledge of the local geology provided by drill holes, and the behaviour of the resistivity as a function of depth outside the geothermal system enabled the construction of an initial 'geologically based' 3-D resistivity model. The initial model was subsequently refined by trial and error fitting of the phase-tensor ellipses using the 3-D finite difference algorithm described by Mackie *et al.* (1994) and Mackie & Booker (1999).

In the central 10-km$^2$ region of Fig. 2, where the data density is greatest, the finite difference grid spacing in the horizontal direction is 250 m. The spacing increases outwards from the central region. In the vertical direction, the depth of the grid nodes increases approximately exponentially between 0.1 and 10 km, coarsening at deeper levels. The mesh spacing in the uppermost 100 m (4 nodes) of the model was chosen to represent the near-surface resistivity structure as determined by central loop transient EM resistivity (TEM) soundings made at each site. The TEM soundings utilize much higher frequencies than the MT data and can resolve the uppermost few hundred metres of resistivity structure, which the MT data cannot. In all, the finite difference grid used $74 \times 68 \times 31$ nodes in the $x$, $y$ and $z$ directions, respectively.

The difficulty with forward modelling with a large numbers of sites is to find an efficient way of comparing the observed and model responses. The approach followed here was to fit maps of phase-tensor ellipses at different periods with corresponding maps of the calculated phase tensors. This approach ensures that the 3-D nature of the data set is honoured, and it also avoids distortion produced by near-surface heterogeneities (geological noise). However, the phase response only contains information on changes or gradients in the resistivity and does not allow the length scale of the resistivity structure to be determined. At Rotokawa, the resistivity information needed to determine the length scale for the forward models is provided by the Schlumberger DC resistivity data and the TEM soundings.

The observed and model phase-tensor maps and induction vectors are shown in Fig. 2. As can be seen in this figure, the main features of the observed phase response are reproduced by the model. Note the high phase at short periods ($T = 0.01$ s) in the centre of the geothermal system, which decreases at longer periods.

The degree of agreement can be assessed more clearly (Fig. 2) using a 'misfit tensor' (Heise *et al.* 2007) to visualize the fit between the modelled and observed phases, where the misfit tensor $\boldsymbol{\Delta}$ is defined here as

$$\boldsymbol{\Delta} = \boldsymbol{I} - \left(\boldsymbol{\Phi}_{\text{obs}}^{-1}\boldsymbol{\Phi}_{\text{mod}} + \boldsymbol{\Phi}_{\text{mod}}\boldsymbol{\Phi}_{\text{obs}}^{-1}\right)/2 \tag{7}$$

and **I** is the identity matrix. The size and colour of the ellipse indicates the magnitude of the misfit; the colour showing the (arithmetic) mean of the maximum and minimum misfit. Where the misfit is large, the orientation of the ellipse indicates the direction in which

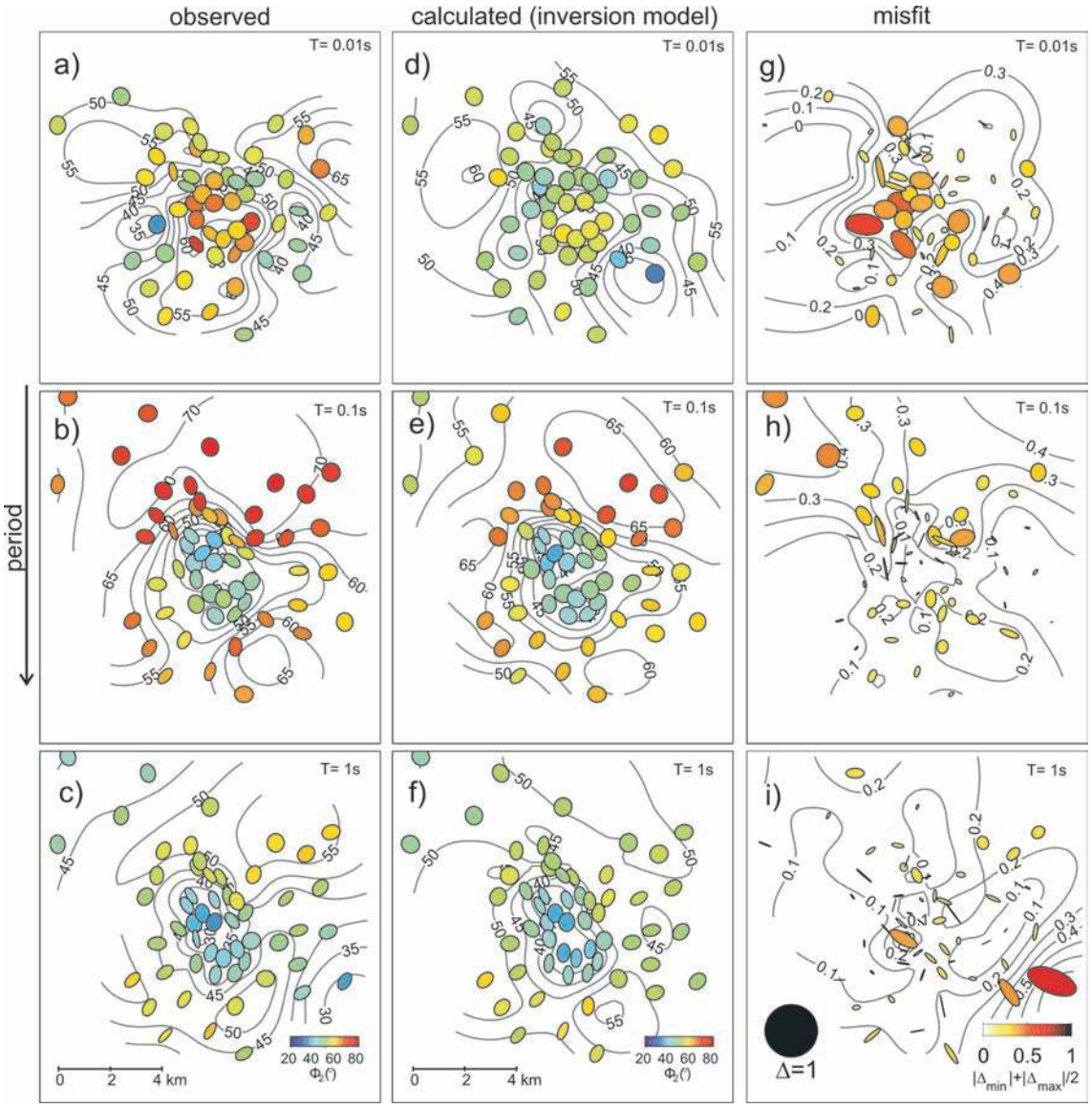


**Figure 3.** (a–c) Phase-tensor ellipses between 0.01 s and 1 s for the sites used in the inversion. The ellipses are normalized with $\Phi_{max}$ and the colours show $\Phi_2 = \sqrt{\Phi_{min}\Phi_{max}}$. (d–f) Calculated phase response from the 3-D inverse model, main features of the data, are reproduced at all periods. (g–i) Tensor misfit $\boldsymbol{\Delta}$ ellipses calculated for the observed and calculated phase tensors of the inversion. The colour used to fill the ellipses shows the mean of the maximum and minimum misfit: $(|\Delta_{max}|+|\Delta_{min}|)/2$.

the difference between the observed and model phases is greatest. At short periods (0.01 and 0.1 s), the misfit tensors are small and orientations are random suggesting that the model has captured the main features of the data. However, at 1 s the ellipses in the south-eastern half of the survey area take on a NW–SE alignment approximately perpendicular to the SE margin of the TVZ suggesting that the conductance of the material overlying the basement has been underestimated in the model.

The induction vectors shown in Fig. 2 provide an independent check of the fit. In general, the direction and amplitude of the calculated induction vectors match those of the observed data.

## 3-D INVERSE MODELLING

3-D inverse modelling was carried out using the code WSINV3DMT described by Siripunvaraporn *et al.* (2005). At present, this code inverts only the impedance tensor data and does not include the induction vector data. Data at 58 sites (Fig. 3) were used for the 3-D inversion, omitting the six noisiest soundings (sites badly affected by electric fences where data at only a few periods were available) and obvious outliers in the remaining soundings. These data were then interpolated at 2 points per decade in a 0.01–30 s period range (i.e. 8 period values). Rather than interpolate error estimates for the observed data, a constant 5 per cent error was assumed for the interpolated impedances. In contrast to the forward modelling, where we attempt to fit only the phase-tensor ellipses (the resistivity scale being provided by the DC apparent resistivity and TEM sounding data), the inversion model fits all of the components of the impedance tensor, i.e. it fits both the apparent resistivity (magnitude) and phase response simultaneously.

Since the impedance tensor may be galvanically distorted and therefore spatially aliased by small-scale near-surface structure (which cannot be modelled with the discretization grid used), distortion should be removed from the impedance data before inversion.

For soundings where the phase-tensor analysis identifies a 1-D section at short periods, galvanic distortion can be removed using the method of Bibby *et al*. (2005a). This method retrieves the shape of apparent resistivity sounding curves but not the resistivity scale, which cannot be determined from the MT data. After distortion removal using this method the resistivity scale was set by comparison with TEM soundings made at each MT measurement location and cross-checked with the Schlumberger apparent resistivity data.

In cases where the phase-tensor analysis at short periods indicated that the near-surface structure was not 1-D (i.e. the 15 sites where the phase-tensor ellipses in Fig. 3a are not circular) an *approximate* resistivity was determined by shifting the (off-diagonal component) apparent resistivity soundings curves. The magnitude of the shift required was determined by matching pseudo MT apparent resistivity sounding curves calculated from 1-D layer model inversions of the TEM soundings. Shifts of less than half a decade were required.

The finite difference mesh was designed so that the discretization in the central part of the model was regular, with a cell width of 400 m, the maximum cell width possible for this distribution of measurement sites. The mesh consisted of a total of 54 cells in both the *x*- and *y*-directions and 24 cells in *z*-direction. Site positions were adjusted slightly so that sites are located at the centre of a cell, as required by the version of WSINV3DMT used. Default values ($\tau = 5$ and $\delta = 0.1$) were used for the two parameters that determine the decorrelation scale that controls the model roughness (Siripunvaraporn *et al.* 2005). Starting from a 100 Ωm uniform half-space, the inversion reached a normalized rms of 5.77 after six iterations and 196 hr of computation time on a Dual-Core AMD Opteron (2.2 GHz) workstation. The memory required for this model was ∼2.5 GB.

Fig. 3 shows the phase-tensor ellipses for the impedance tensor data used in the inversion, the phase response from the final inversion model and the misfit tensors. Compared with the forward model results, phases at 0.01 s in the centre of the geothermal system are significantly lower in the inverse model. This difference is a consequence of a thin (15 m) resistive (200 Ωm) layer at the surface that was included in the forward model to match the high phases observed at the shortest periods but which cannot be accurately represented with the slightly coarser near-surface discretization used in the inversion model.

At 0.1 and 1 s (Fig. 3) the calculated and observed phase-tensor ellipses are in a good agreement as can be seen in the corresponding misfit tensor plots. At 1 s, the orientations of the misfit ellipses appear random and are smaller than the corresponding misfit ellipses for the forward model. Thus, the inverse modelling has done a better job of fitting the orientation of the phase-tensor ellipses at this period.

In Fig. 4, we show the misfit tensor maps for different iterations at three selected periods. These maps show the progress of the inversion, with the misfit ellipses providing a visualization of the signal used to 'drive' the inversion. This is most clearly seen at 3-s period where, for the initial model, the misfit ellipses are large and oriented perpendicular to the strong resistivity gradient at depth associated with the SE rift margin. As the inversion proceeds, the phase-tensor residuals become small. After iteration 4, (rms 5.98) improvement in the phase fit is barely visible, although the overall rms, which includes the amplitude or apparent resistivity data, decreases to 5.77.

## RESULTS AND DISCUSSION

Figs 5–7 show a comparison of the forward and inverse models. The distribution of resistivities is similar. At shallow depth (15–200 m) the geothermal field is characterized by low resistivities (1–5 Ωm) in the inverse model, in a good agreement with the Schlumberger resistivity data. Outside the geothermal system the top 500 m of young volcanics are resistive (300 Ωm), but become more conductive (30–10 Ωm) below about 600 m. Inside the geothermal system, beneath the shallow low-resistivity zone near the surface, resistivity in both models increases to ∼30 Ωm at ∼300 m depth then decreases again to <10 Ωm at ∼500 m depth. The resistivity then increases to values >100 Ωm at depths greater than 1200 m.

One of the major differences between the models is the resistivity of the conductive volcanics, shown most clearly in the 800-m-depth slice (Figs. 5b and f). In the forward model, a SW–NE band of conductive volcanics (8 Ωm) seen in the 800-m-depth slice was included on geological grounds. The inversion model suggests that the resistivity of this material at the margins of the geothermal system is significantly lower (1–8 Ωm). This can be seen in the 3-D cutaway picture of the conductivity structure in Fig. 7. In the forward model the greater conductance at the margins of the geothermal field is modelled as a thicker layer of 8 Ωm.

In both the forward and inverse models a narrow resistive feature along the western side of the geothermal system about 800 m deep (Figs. 5b and f) is necessary to produce the elongated phase-tensor ellipses that occur in the area above the resistor at periods between about 0.1 (Fig. 3b) and 0.5 s.

An unexpected feature of the forward modelling was the high resistivity needed to model the decrease in phase seen in the central part of the geothermal field (Fig. 5c). Hypothesis testing indicated that a resistive zone (>300 Ωm) of limited extent between 900- and 2400-m depth was necessary to reproduce the low $\Phi_{min}$ values observed between 0.1 and 1 s period. However, since the phase reflects only the resistivity contrast, if the resistivity value of the overlying conductive material is lower, the resistivity of this body will also be lower as the inversion model suggests.

Changes in resistivity in a convective geothermal system like Rotokawa will be the result of the interplay of temperature, fluid chemistry and porosity, all of which play a large role in determining the nature of the alteration products (clays) and thus the resistivity inside and at the margins of the geothermal system. Fig. 6 shows an N–S temperature profile of the geothermal system overlying resistivity sections of forward and inverse model.

At shallow levels (<500 m), the high conductivity that occurs in the TVZ's geothermal systems is usually attributed to the presence of conductive hydrothermal alteration products, (clays). The alteration products form a conductive cap above a more resistive, higher temperature reservoir (Björnsson *et al.* 1986; Pellerin *et al.* 1996; Ussher *et al.* 2000). In particular, between 70 °C and 200 °C hydrothermal alteration produces smectites that have a very high cation exchange potential, which reduces the resistivity markedly. Also, at shallow levels, geothermal fluids are often acidic due to the presence of $HCO_3$- or $SO_4$-rich waters. At Rotokawa, a 300-m-thick high conductivity layer near the surface corresponds with high-porosity lacustrine and volcaniclastic sediments that contain acidic ground waters, consistent with the low resistivity modelled. The increase in resistivity to ∼30 Ωm seen in the models between 300 m and 500 m depth (Figs 6 and 7) may be related to an inflow of cooler and near-neutral ground waters (known from drill holes) in the northern part of the geothermal system. The complicated temperature distribution in the southern part of the geothermal system (Fig. 6) may be partly caused by the shallow reinjection of wastewater in this area. If so, then alteration products and resistivity may not reflect the present temperature distribution but rather the temperature/alteration pattern prior to reinjection.

As temperatures increase to ∼200 °C with increasing depth, this material becomes more conductive again as the amount of smectite

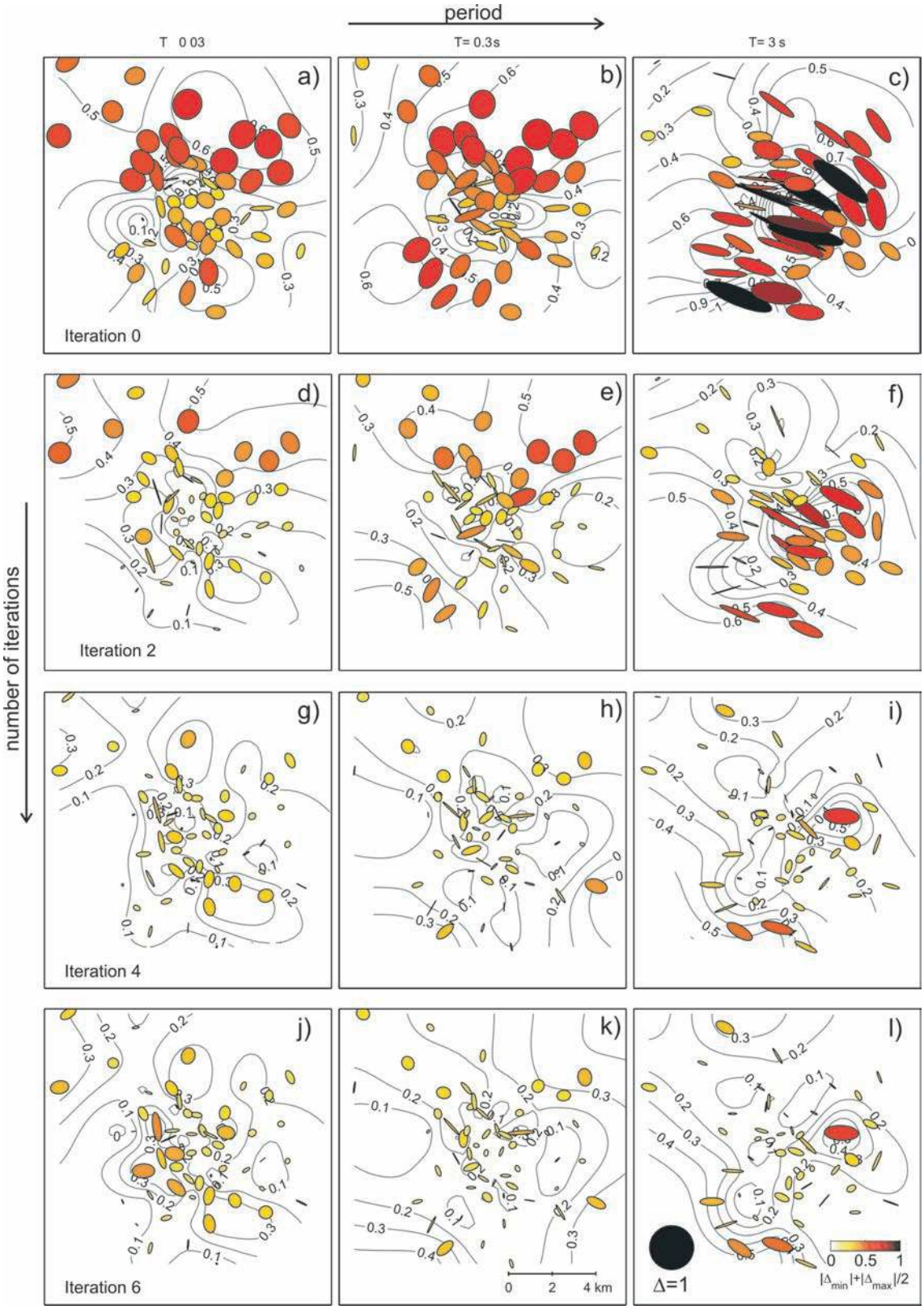


**Figure 4.** Tensor misfit ellipses for the observed and calculated phase tensors of the inversion for four iterations at three different periods. Iteration 0 shows the misfit of a homogenous half space of 100 Ωm. Note the systematic direction of the misfit ellipses for iteration 0 at 3 s reflecting difference between the initial model (a uniform half-space) and the quasi-2-D regional conductivity structure of the TVZ.

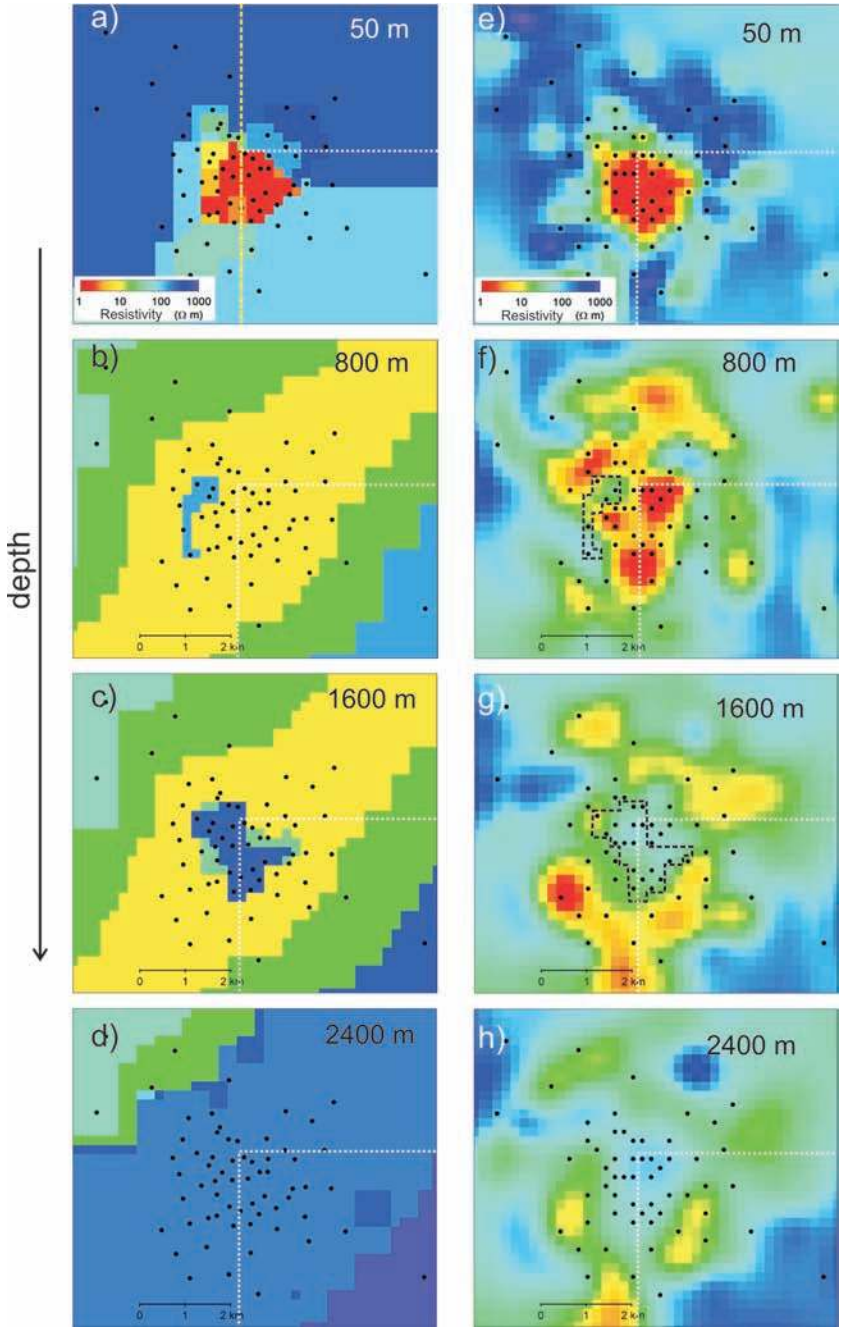


**Figure 5.** Resistivity maps 3-D models at four different depths. Dots show MT sites used for the modelling; (a–d) forward model, (e–h) inverse model (6th iteration). The dashed black lines in f and g mark the resistive bodies of the forward model at 800 m and 1600 m depth. The yellow dotted line in (a) marks the location of the resistivity section of Fig. 6. The white dotted lines indicate the edge of the 3-D cut away shown in Fig. 7.

increases. On the flanks of the geothermal system, where temperatures will be lower and fluids are less saline and acidic than at similar levels within the geothermal system, the smectite stability zone and corresponding conductive zone will extend deeper, as suggested by the inversion model (Fig. 7b).

At a depth of ∼1200 m, where temperatures exceed 250 °C in the centre of the geothermal field, the resistivity starts to increase. At these higher temperatures, alteration products are less-conductive illitic and chloritic clay minerals. Porosity also decreases, due to compaction of volcaniclastic sediments and because the sediments give way to low-porosity andesitic lava at deeper levels. The resistivity however also depends on the alteration history, e.g. the discrepancy between the 250 °C isotherm and the resistive body (Fig. 6b) in the southern part of the section could be caused by changes of the temperature distribution with time.

The hottest part of the geothermal system (known from drilling) correlates with the high-resistivity zone within the volcaniclastic material in the centre of the models (Figs 5–7); in broad agreement with resistivity structure expected from the temperature dependence of the hydrothermal alteration products.

The NW dipping resistive basement first appears in both models at about 1600-m depth. At 2400-m depth, the inverse model has lower basement resistivities (∼300 Ωm) than the forward model (500–1000 Ωm). Although poorly resolved, the resistivity

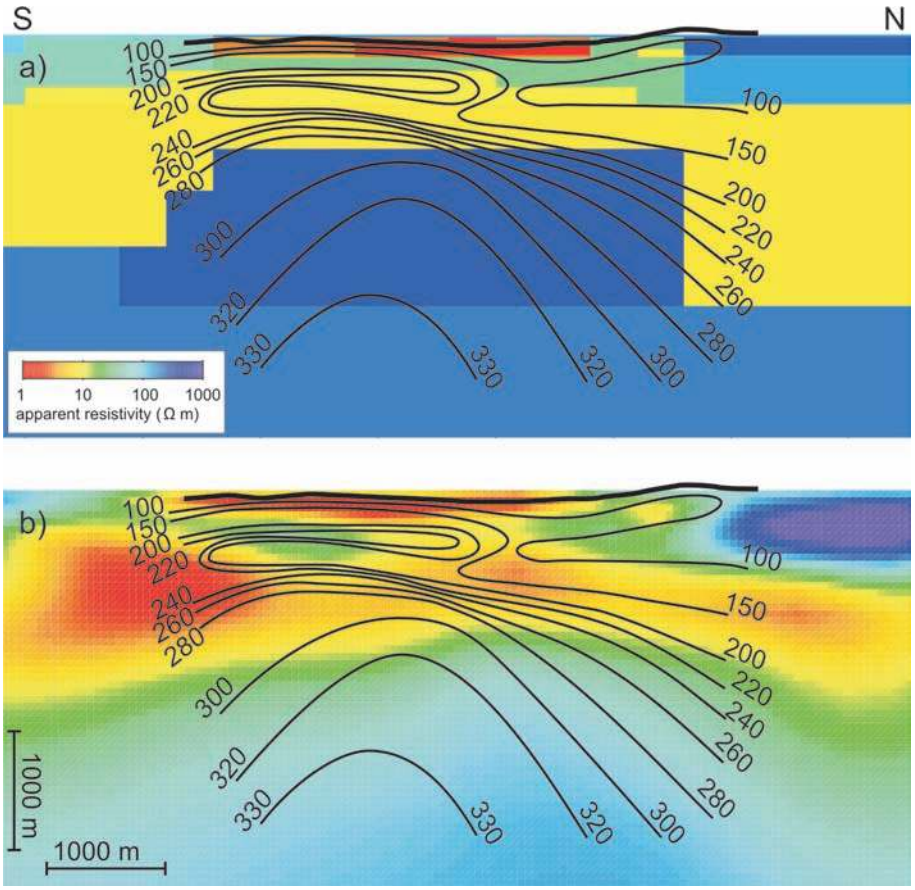


**Figure 6.** Resistivity section through the centre of the geothermal system (a) forward model; (b) inverse model. Isotherms, interpolated from wells measurements, show the temperature distribution inside the geothermal system. The complicated temperature structure of the near surface may partly reflect the reinjection of wastewater in the top 500 m. In the northern part the low temperatures ($<100\,^{\circ}$C) at $\sim$500 m depth can be explained by an inflow of cold water from the resistive rhyolite dome north of the geothermal system. At depth the higher resistivity corresponds to temperatures $>250\,^{\circ}$C.

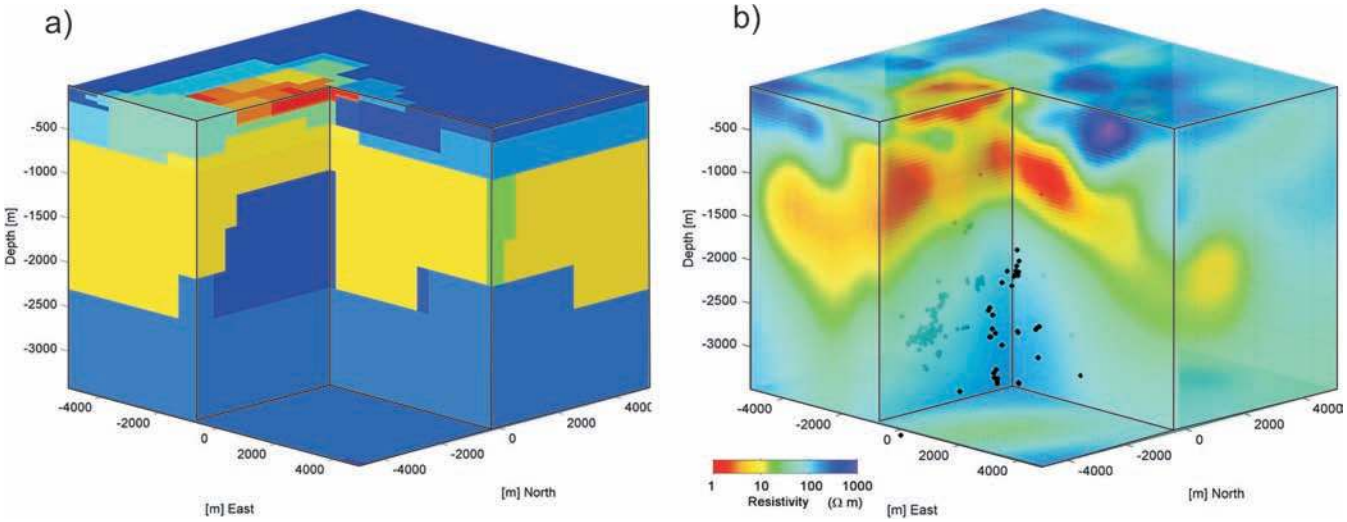


**Figure 7.** 3-D perspective views of forward (a) and inverse (b) modelling results. Earthquake locations are shown as black dots in the partial transparent conductivity model. Nearly all of the earthquake hypocentres lie within the bounds of the deep resistive body (given location uncertainties of *ca*.200 m).

beneath the central part of the geothermal field in the inverse model appears to be more resistive than the adjacent basement rocks that have low resistivities ($\sim$30 Ωm in Fig. 5). Heise *et al.* (2007) found that resistivity values of the basement in a band along the SE margin of the TVZ are low, but not as low as suggested by the inversion model. Unfortunately, the coverage of measurements around the geothermal system makes the significance of this structure uncertain. Further development of the inversion code to include induction vector data may also help resolve this feature.

## CONCLUSIONS

The deep high-temperature parts of a geothermal system are the ultimate target of geothermal drilling for electric power production. Generally, the reservoir is marked by higher resistivity beneath a cap of highly conductive material produced by hydrothermal alteration of the host rock and a core of higher resistivity material marking the highest temperature part of the geothermal system. Both the forward and inverse modelling of MT data from Rotokawa support this interpretation of the conductivity structure within the rhyolitic volcanics.

The similarity of the forward model with the inverse model gives confidence in the results of the 3-D inversion in regions where the measurement density is high. However, even with the large number of stations available at Rotokawa, the conductivity structure of the deeper parts (>2.5 km) of the geothermal system remains poorly resolved. Further measurement in the region surrounding the geothermal field would help increase the resolution of the structure at depth.

The most interesting feature of the modelling is the high-resistivity body in the central part of the geothermal field. This feature correlates spatially with the zone of highest temperature and extends into the andesite and basement greywacke at deeper levels. Hypocentres of micro-earthquakes ($M_L$ − 0.4 to 1.7) induced by re-injection of waste fluid recorded over two months by a 10-station surface seismometer array are shown in Fig. 7(b). Location errors in the hypocentres are small, ∼200 m. As can be seen in Fig. 7(b) the earthquakes occur within the zone where the high-temperature hydrothermal alteration minerals are resistive. Since the permeability at deeper levels in the greywacke and andesite is expected to be fracture dominated, the correlation of the high resistivity and seismicity suggests that the MT data are imaging the resistivity signature associated with zones of fracture permeability that are feeding high-temperature fluid into the geothermal system from below.

One of the important lessons of our work at Rotokawa is that conventional methods of MT analysis have limited applicability when the situation is strongly 3-D. We believe the coordinate invariant approach we have followed for the forward modelling and the use of phase-tensor ellipses to visualize both the model results and the misfits is an example of how the problem of 3-D MT modelling of complicated 3-D resistivity structures can be approached. The consistency of the forward and inverse models, and their geological plausibility, suggests that our approach has been successful in this case.

## ACKNOWLEDGMENTS

Geosystems SRL collected and processed the MT and TEM data. We would like to thank the Rotokawa Joint Venture for supplying MT and TEM data and for giving permission to publish these results. In addition, we would like to acknowledge Tom Powell and Luis Urzua at Mighty River Power Ltd for their encouragement and support of this research. Comments from Max Moorkamp, Gerard Muñoz and Oliver Ritter helped to improve clarity of this manuscript. We thank Weerachai Siripunvaraporn for supplying his 3-D inversion code.

## REFERENCES

Arehart, G.B., Christenson, B.W., Wood, C.P., Foland, K.A. & Browne, P.R.L., 2002. Timing of volcanic, plutonic and geothermal activity at Ngatamariki, New Zealand, *J. Volcanol. Geotherm. Res.,* **116,** 201–214.

Bannister, S. & Melhuish, A., 1997. Seismic scattering and reverberation, Kaingaroa plateau, Taupo Volcanic Zone, New Zealand, *N. Z. J. Geol. Geophys.,* **40,** 375–381.

Bibby, H.M., 1986. Analysis of multiple-source bipole-quadripole resistivity surveys using the apparent resistivity tensor, *Geophysics,* **51,** 972–983

Bibby, H.M., 1988. Electrical resistivity mapping in the central volcanic region of New Zealand, *N. Z. J. Geol. Geophys.,* **31,** 259–274.

Bibby, H.M. & Hohmann, G.W., 1993. Three-dimensional interpretation of multiple-source bipole-dipole resistivity data using the apparent resistivity tensor, *Geophys. Prosp.,* **41,** 697–723.

Bibby, H.M. & Risk, G.F., 1973. Interpretation of dipole-dipole resistivity surveys using a hemispheroidal model, *Geophysics,* **38,** 719–736.

Bibby, H.M., Caldwell, T.G., Davey, F.J. & Webb, T.H., 1995. Geophysical evidence on the structure of the Taupo Volcanic Zone and its hydrothermal circulation, *J. Volcanol. Geotherm. Res.,* **68,** 29–58.

Bibby, H.M., Caldwell T.G. & Risk, G.F., 1998. Electrical resistivity image of the upper crust within the Taupo Volcanic Zone, New Zealand, *J. Geophys. Res.,* **103,** 9665–9680.

Bibby, H.M., Caldwell, T.G & Brown, C., 2005a. Determinable and non-determinable parameters of galvanic distortion in magnetotellurics, *Geophys. J. Int.,* **163,** 915–930.

Bibby, H.M., Risk, G.F., Caldwell, T.G. & Bennie, S.L. 2005b. Misinterpretation of electrical resistivity data in geothermal prospecting : a case study from the Taupo Volcanic Zone. 8p, in *Proceedings of the World Geothermal Congress 2005, Antalya, Turkey*.

Björnsson, A., Hersir, G.P. & Björnsson, G., 1986. The Hengill high-temperature area, S.W. Iceland: regional geophysical survey, *Geotherm. Resour. Counc. Trans.,* **10,** 205–210.

Caldwell, T.G., Bibby, H.M. & Brown, C., 2004. The magnetotelluric phase tensor, *Geophys. J. Int.,* **158,** 457–469.

Heise, W., Bibby, H.M., Caldwell, T.G., Bannister, S.C., Ogawa, Y., Takakura, S. & Uchida, T., 2007. Melt distribution beneath a young continental rift: the Taupo Volcanic Zone, New Zealand, *Geophys. Res. Lett.,* **34,** L14313, doi:10.1029/2007GL029629.

Hunt, T.M. & Harms, C. 1990. Gravity Survey of the Rotokawa Geothermal Field, in *Proceedings of the 12nd New Zealand GEOTHERMAL Workshop*. University of Auckland, Auckland.

Jiracek, G.R., 1990. Near-surface and topographic distortions in electromagnetic induction, *Surv. Geophys.,* **11,** 163–203.

Larsen, J.C., Mackie, R.L., Manzella, A., Fiordelisi, A. & Rieven, S., 1996. Robust smooth magnetotelluric transfer functions, *Geophys. J. Int.,* **124**, 801–819

Mackie, R.L. & Booker, J., 1999. Documentation for mtd3fwd and d3-to-mt, GSY-USA, Inc., 2261 Market St., Suite 643, San Francisco, CA 94114. *User documentation*.

Mackie, R.L., Smith, J.T. & Madden, T. R. 1994. Three-dimensional electromagnetic modeling using finite difference equations: the magnetotelluric example, *Radio Sci.,* **29,** 923–935.

Ogawa, Y., Bibby, H.M., Caldwell, T.G., Takakura, S., Matsushima, N., Bennie, S.L., Tosha, T. & Nishi, Y., 1999. Wide-band magnetotelluric measurements across the Taupo volcanic zone: preliminary results, *Geophys. Res. Lett.,* **26,** 3673–3676.

Parkinson, W.D., 1962. The influence of continents and oceans on geomagnetic variations, *Geophys. J. R. astron. Soc.,* **6,** 441–449.

Pellerin, L., Johnston, J.M. & Hohmann, G.W., 1996. A numerical evaluation of electromagnetic methods in geothermal exploration, *Geophysics*, **61,** 121–130.

Risk, G.F., 1983. Delineation of geothermal fields in New Zealand using electrical resistivity prospecting, in *Proceedings of the Third Biennial Conference of the Australian Society of Exploration Geophysicists*, pp. 147–149.

Risk, G.F., 2000. Electrical resistivity surveys of the Rotokawa geothermal field, New Zealand, in *Proceedings of the 22nd New Zealand Geothermal Workshop*, pp. 121–126, eds Dunstall, M.G., Morgan, O.E. & Simmons, S.F., University of Auckland, Auckland.

Siripunvaraporn W., Egbert, G., Lenbury, Y. & Uyeshima, M., 2005. Three-dimensional magnetotelluric: data space method, *Phys. Earth Planet. Inter.,* **150,** 3–14.

Stanley, W.D. Mooney, W.D. & Fuis, G.S. 1990. Deep crustal structure of the Cascade range and surrounding regions from seismic refraction and magnetotelluric data, *J. Geophys. Res.,* **95,** 19 419–19 438.

Ussher, G., Harvey C., Johnstone, R. & Anderson E., 2000. Understanding resistivities observed in Geothermal Systems, in *Proceedings World Geothermal Congress 2000*, Kyushu-Tohoku, Japan.

Wilson, C.J.N., Houghton, B.F., McWilliams, M.O., Lanphere, M.A., Weaver, S.D., & Briggs, R.M., 1995. Volcanic and structural evolution of Taupo Volcanic Zone, New Zealand: a review, *J. Volcanol. Geotherm. Res.,* **68,** 1–28.